Chapter 5

OSIRIS IFU View of Submillimeter Galaxies: a 2-D Spectroscopic Insight to Starburst Galaxies in the High-Redshift Universe

We target Hα emission of three *submillimeter* galaxies (SMGs) at mean redshift, $< z > \sim 2.0$ with the OH-Suppressing Infrared Imaging Spectrograph (OSIRIS) in conjunction with the Keck Laser-Guide Star Adaptive Optics system. This spatially-resolved spectroscopic insight into the kpc-scale structure of these galaxies, reveals that the Hα emission in SMGs extends over scales $\sim 0.5'' - 2.0''$ or $4 - 17$ kpc. We distinguish spatially compact, broad-Hα line regions associated with an AGN and the extended regions of star formation traced by narrow-line Hα emission. This allows us to refine significantly estimates of stellar dynamical masses and star-formation rates (SFR) for the SMG population, which are critical for imposing constraints to current models of galaxy formation, but in the past inevitably hampered by both AGN contamination of emission lines and incomplete spatial sampling in long-slit spectroscopic studies. We also explore the dynamics of gas in the inner galaxy halo to improve our understanding of the internal dynamics of this enigmatic galaxy population. We find no evidence of ordered orbital motion, but rather large velocity offsets ($\sim$ *few* $\times$ 100 km s^{-1}) between distinct galactic-scale sub-components. Considering the disturbed morphology of SMGs, these sub-components are likely remnants of originally independent gas-rich galaxies that are in the process of merging, hence

triggering the ultraluminous SMG phase. Our Hα-based results are consistent with those derived from high-resolution CO observations, with $M_{dyn} \sim 4 - 20 \times 10^{10}$ $M_\odot$. We find that SMGs host SFR surface densities $\Sigma_{\rm SFR} \sim 4 - 20$ $M_\odot$ yr^{-1} kpc^{-2}, a factor of $\sim 2 - 6$ higher than the median value for optically-selected high-redshift galaxies, but similar to local ULIRGs and circumnuclear starbursts.

5.1   Introduction

The details of stellar mass assembly are crucial for a full understanding of galaxy evolution. Most of the present-day stellar mass was already in place at $z \sim 1$, and the bulk of stellar build-up apparently took place at $1 \lesssim z \lesssim 2.5$ (e.g., Dickinson et al. 2003). Within this redshift range, galaxies grow rapidly to attain their final stellar masses. With inferred SFRs $\gtrsim 100 - 1000$ $M_\odot$ yr^{-1}, SMGs could build the stellar bulk of a massive galaxy in under a few hundred million years.

At $z \sim 2$, the large stellar masses associated with SMGs ($\sim 10^{11}$ $M_\odot$; Borys et al. 2005) represent important constraints in models of galaxy formation. Furthermore, they have led to the claim of a possible top-heavy IMF to reconcile SFRs at $z \sim 2$ with the masses of local massive ellipticals (Baugh et al. 2005). However, the SMG stellar mass estimates rely on fitting SED to near-IR and optical aperture photometric data (Borys et al. 2005) and recent work by Maraston et al. (2006) suggests that there is significant uncertainty associated with the assumed stellar ages and thus on photometric mass estimates derived for high redshift galaxies.

As discussed in Chapter 4, deep long-slit spectroscopic observations of Hα emission in SMGs with the Near-Infrared Spectrograph (NIRSPEC) on Keck have also provided further constraints to the dynamical masses inherent to this population: S04 find a median value of $\simeq (1.5 \pm 0.9) \times 10^{11}$ $M_\odot$ for a sample of 30 SMGs. Moreover, S04 report that broad Hα emission (FWHM$_{H\alpha} \gtrsim 1000$ km s^{-1}) is present in $\gtrsim 40\%$ of their SMG sample and that the composite spectrum of their sample is best represented by a narrow Hα line and an underlying broad Hα component with narrow-to-broad-line flux ratio of 0.6 ± 0.1 and with FWHM$_{rest} = 325 \pm 30$ and

1300 ± 210 km s^{-1}, respectively. The broad Hα line is due to the large velocities within the broad-line region close to a central AGN. Dynamical mass estimates based on the width of the Hα line thus retain the substantial caveat that broadening and brightening of the Hα emission due to the blended nuclear emission from an AGN may result in overestimates. When both AGN and star-forming activity are present, long-slit spectroscopic techniques face difficulties in disentangling their independent contributions, and may result in wrong estimates of the SFRs and dynamical masses of SMGs. The S/N of Hα NIRSPEC long-slit observations is sufficient to detect a clear AGN-like broad line signature, but is inadequate to reliably quantify the AGN contribution (S04). Therefore, SFRs and dynamical masses of SMGs may both be overestimated. Furthermore, dynamical information has also proved difficult to extract from NIRSPEC data (S04), even for the less extreme and likely more ordered cases of optically-selected LBGs at similar redshifts (Erb et al. 2003).

Integral field spectroscopy opens the possibility of investigating the properties of nebular emission at different scales within a galaxy. A two-dimensional (2D) spatial spectroscopic insight to the line emission is the only viable probe of the distribution and dynamics of the gas in the inner galaxy, on $1 - 10$ kpc scales. The 2D velocity fields can cast new light on the nature of these galaxies, whether consisting of gas forming stars in a disk or a merger between galaxies.

Results from the SPectrometer for Infrared Faint Field Imaging (SPIFFI) on the ESO Very Large Telescope (VLT) first showed how 2D spectroscopy could reveal structure in line emission across a dusty galaxy at $z \simeq 2.5$ (Tecza et al. 2004). Their marginally resolved (non-AO) spectra reveal substructure in nebular and continuum emission. Using the relatively modest $0.2''$ resolutions $R \simeq 1000, 1700$ of the integral-field unit (IFU) at UKIRT (UIST) and the Gemini Near-IR Spectrograph (GNIRS) IFU at Gemini-South, respectively, Swinbank et al. (2006) (hereafter, S06) investigated the 2D spectra of six SMGs at $z = 1.3 - 2.5$. They detected kpc-scale Hα sub-structure, including multiple components and extended emission. The OH-Suppressing Infrared Imaging Spectrograph (OSIRIS; Larkin et al. 2006) on Keck II benefits from superior spectral resolution ($R \simeq 3000 - 3800$) and a larger tele-

Table 5.1. Summary of *OSIRIS* Observations

Name	RA[a] (*h m s*)	Dec. (° ′ ″)	$z_{optical}$	Filter	Plate Scale mas	Exposure times ks	Date
SMM J030227.73[b]	03:02:27.73	+00:06:53.5	1.4076[c,d]	*Hn2*	100	12.6	Oct. 2005
SMM J123549.44[e]	12:35:49.44	+62:15:36.8	2.2032[c]	*Kn2*	50	10.8	May 2007
SMM J163650.43[f]	16:36:50.43	+40:57:34.5	2.3850[c]	*Kn3*	50	12.6	May 2007

[a] Radio center from C05

[b] Tip-tilt star 03:02:25.19 +00:06:43.80, with *R*-mag= 17.8 and 39.3″ separation.

[c] From S04

[d] From S06

[e] Tip-tilt star 12:35:43.33 +62:14:56.69, with *R*-mag= 15.0 and 58.6″ separation.

[f] Tip-tilt star 16:36:50.61 +40:56:50.92, with *R*-mag= 13.7 and 43.6″ separation.

scope (10-m). Moreover, OSIRIS is designed to be used with the Keck Laser-Guide Star Adaptive Optics (LGS-AO; Wizinowich et al. 2006; van Dam et al. 2006) system, which allows for atmospheric distortion corrections to be derived from parallel observing of a nearby bright star and applied to the science targets. Adaptive Optics thus enables diffraction-limited resolution to be reached with ground-based observations to probe for kpc-scale structures in galaxies at $z \sim 2$.

In this chapter we present the results of an OSIRIS program that we have undertaken to study the 2D distribution of Hα emission of three SMGs from the radio-identified sample of C05. We discuss our sample selection and observing strategy in §5.2. The steps comprising the reduction and analysis of the science spectra are discussed in §5.3. Our results are presented in §5.4 and discussed in §5.5.

5.2 Observations

We obtained our observations from October 2005, during the shared-risk science period of the OSIRIS instrument, to March 2008. Observing conditions varied from photometrically optimal, with $\sim 0.4''$ seeing in the V-band, to moderate, with a seeing $\sim 1''$.

The integral field capability of OSIRIS is based on an array of 3000 lenslets, each

of which produces a spectrum of a different location of the observed target. In this way, OSIRIS spectroscopically *dissects* the 2D-image of a galaxy. To optimize the detection of our targets, we selected SMGs with bright Hα lines, detected in previous long-slit spectra (S04; Takata et al. 2006). LGS-AO allows for corrections to be derived for targets with a $tip-tilt$ star that can be as faint as $R \sim 18$ within $1'$ of the science target. Taking all these considerations into account, we selected our science targets carefully to optimize OSIRIS performance.

5.2.1 Sample Selection

We selected our SMG targets from the sample of SMGs in C05. We took advantage of existing near-IR long-slit Hα spectroscopy (S04, Takata et al. 2006) to select those SMGs with the brightest Hα lines, $S_{H\alpha} \gtrsim 10^{-15}$ erg s^{-1} cm^{-2} to optimize detection. For the tip-tilt star selection we used the Keck Adaptive Optics Guide Star online tool [1] and corroborated the quality of the tip-tilt star candidates (stellar nature and magnitude) using the Sloan Digital Sky Survey Catalog Archive Server (Adelman-McCarthy et al. 2008).

We also selected SMGs with Hα emission lines that did not fall on bright near-IR OH sky emission lines. The resulting sample of SMG targets, complying with these requirements are listed in Table 5.1.

5.2.2 Instrument Configuration and Observing Strategy

The targets in our sample have redshifts from $z \simeq 1.4$ to $z \simeq 2.4$, which places their observed Hα emission in the $H-$ and $K-$band.[2] In the interest of obtaining the largest field of view available at the observed Hα wavelengths, we used the narrow-band filters indicated in Table 5.1.

Our observations include a combination of the 100-mas and the 50-mas plate-

---

[1] http://www2.keck.hawaii.edu/software/findChartGW/acqTool.php

[2] AO corrections in the $J-$band are not optimal. The *strehl* value for a given wavelength gives a measure of the quality of the LGS-AO corrections and is given by: $S = e^{-(2\pi\sigma/\lambda)^2}$; therefore, as λ decreases, so does the AO correction.

scales, which provide the largest fields of view (FOV): $\sim 4.8'' \times 6.4''$ and $\sim 2.4'' \times 3.2''$, respectively. The 100-mas lenslet plate-scale has the advantage of allowing us to maximize the area of photon collection, crucial for the study of faint objects. However, the background thermal noise for this coarsest plate-scale had been significantly underestimated (Law et al. 2006); instrument servicing on February 2006 included a decreased pupil size for the $0.05''$, $0.035''$ and $0.02''$ plate-scales, leading to a significant decrease in thermal background. Thereafter, we used the $50-$lenslet scale to benefit from the reduced instrument background to improve our science detections at the cost of a reduced FOV.

Our observing strategy consists of an initial pair of spectroscopic frames offset from one another by $0.5''$ on the tip-tilt star. These short-exposure frames ($\sim 1 - 10$ s) were used as a coordinate centering reference. Having calculated precise offsets to the science target from deep $K-$band images (e.g., Smail et al. 2004), we do a blind-offset to the science target. These consist on sets of standard ABBA sequences separated by tiny offsets ($\pm 0.5''$) followed by a sky-integration frame, offset by $\sim \pm 15''$ from the science target. Each ABBA sequence comprises four $15-$minute frames taken at two positions separated by $0.5''$ to allow for on-object dithering. Our strategy required a large number of dark frames, taken during the afternoon prior to and in the morning after the observing night. These darks have the same exposure times as the science exposures.

5.3   Reduction and Analysis

We use the OSIRIS Data Reduction System (DRS) pipeline[3] to do the basic reduction of all science and calibration data. The pipeline consists of an IDL-based program comprising a collection of individual modules, each of which performs a specific task and which we can optionally include or exclude at different pipeline *passes*. OSIRIS raw files are multi-extension fits files, with the image data contained in the 0th extension, the standard deviation of sampling in the 1st and the data quality (bad pixel

---

[3]http://www.astro.ucla.edu/~irlab/osiris/pipeline.html

mask) on the 2nd. Key information, including telescope pointing information for each exposure, is included in the data headers. The major reduction steps of the pipeline are: subtraction of a dedicated sky frame from each science exposure, transformation of a *raw* 2D file into a three-dimensional (3D) data cube and the mosaicing of all science frames into one single data cube. The resulting 3D data cube has two spatial axes (x, y) and a third axis for wavelength (λ), calibrated according to the corresponding rectification matrix available for the particular instrument setup (filter and lenslet plate-scale). We refer the reader to the OSIRIS Manual [4] for a detailed description of the pipeline.

The science targets in our program are faint and potentially significantly extincted sources. Their analysis thus requires a series of reduction steps in addition to the standard pipeline processing to minimize the otherwise persistent sky background. In particular, we perform additional corrections to remove instrument artifacts (a simulated flat-fielding) and sky subtraction. These additional reduction steps are tuned carefully to each object.

The OSIRIS pipeline assumes that any signal in the image corresponds to photons from the science target. Any charge accumulation on the detector or any other spurious signal of different nature will therefore be interpreted as part of the science detection. To get rid of these artifacts we simulate a flat-fielding of the science data cubes. For this, we pipeline-process the individual dedicated sky exposures by subtracting a *master*-dark image from each sky frame, where the *master*-dark image results from median-combining the collected dark frames. For the standard sky-subtraction step within the OSIRIS pipeline, we use the processed sky cube taken within the shortest time from the science exposure (the *nearest* sky frame).

In addition to this standard sky subtraction, we perform two additional steps of sky subtraction. In the case of faint targets, such as the ones in our sample, residual background from the OH lines after sky subtraction can be significantly detrimental to our analysis. We first create a *supersky* 2D image, by median-combining the pipeline-reduced sky cubes (without making any offsets with respect to the telescope

---

pointing information in the individual sky frame headers) and wavelength-collapsing the combined cube along the λ-range around where the emission line is expected, $\lambda \simeq \lambda_{H\alpha} \pm 600\,\text{Å}$. We then divide each wavelength slice in the science data cube by this *supersky* image, simulating a flat-fielding of the science image. The second step of additional sky subtraction consists of calculating the median flux for all spatial pixels in each λ-frame in the science data cube and subtracting this value from each (wavelength-slice) frame in the science cube. In this way we set the persistent background to zero, eliminating the residual background plateau within the science cube.

Finally, we mosaic the different science frames using the mean-clip averaging algorithm included in the OSIRIS pipeline. For this, we rely on the RA and DEC header keywords, which remain accurate telescope pointing coordinates throughout observations with uninterrupted LGS acquisition.

In the cases where OH-line background still persisted at a significant level within the mosaiced cube, we also made use of the sky-subtraction routine developed by Davies (2007). This routine is specifically tailored to remove under- and over-subtracted OH-emission from near-IR integral-field spectra, taking into account the temporal variations in absolute fluxes of OH-lines as well as their individual fluxes relative to each other. Although only a modest increase in S/N resulted for the observations presented here ($\lesssim 1.5$), we adopt this routine.

5.3.1 Hα Maps

The major appeal of integral field spectroscopy is that it allows for a 2D spatial insight to the spectral properties of an object. We take advantage of this new view and construct a number of maps to help us understand the distribution of Hα properties across the SMGs in our sample. These include Hα narrow-band (NB) images, and velocity and line-width maps.

With sky-subtracted, flat-fielded, mosaiced science data cubes in hand, we produce NB images collapsed over a range $\Delta v \simeq 1000 - 2000$ km s^{-1} centered at the redshifted

Hα line for each of our targets, assuming redshifts from prior long-slit near-IR spectroscopy (S04), verified against OSIRIS observations. We use these Hα narrow-band images to map the overall distribution of the line emission and to measure the spatial extent of nebular emission throughout the galaxy. In this way, we distinguish between compact and more diffuse regions of emission. The former are likely associated with AGN or compact starburst, while the latter indicate extended star formation. We convert integrated Hα line fluxes at each pixel into a SFR, following Kennicutt (1998):

$$SFR \, [\mathrm{M_\odot \, yr^{-1}}] = 7.9 \times 10^{-42} \times (L_{H\alpha} \, [\mathrm{erg \, s^{-1}}]) \qquad (5.1)$$

The distribution of SFRs across the object is used to build star-formation rate surface density (Σ_{SFR}) maps, considering the pixel scale of the observations. These maps allow us to compare our Σ_{SFR}-values to those found in local star-forming galaxies (Kennicutt 1998) and other high-redshift populations (e.g., LBGs; Erb et al. 2006a). We caution that the AGN contribution to the Hα emission is included in these maps, which we exclude from the SFR quantitative analysis in §5.5.2.

We extract velocity maps for each science cube by fitting gaussian line profiles in the dispersion direction at each pixel location. To improve the S/N in these velocity maps, we first convolve the data along the spatial direction with a 2D gaussian function with FWHM = 2.0 pixels. These velocity maps allow us to probe for velocity offsets between distinct components in each system. We use the gaussian fits at each pixel to re-construct the science detection in terms of S/N maps and to map the distribution of line widths, in terms of the velocity dispersion $\sigma_{rest} = \mathrm{FWHM}_{rest}/2.355$. The latter allows us to probe for the presence of AGNs, as revealed by large line-widths, with $\mathrm{FWHM}_{rest} \gtrsim 1000$ km s^{-1}.

We take advantage of our NIRSPEC long-slit observations (see Chapter 4; S04) to provide an *approximate* flux calibration to the Hα line in our data cubes. For this, we collapse each data cube along the dispersion direction within a $\Delta\lambda \sim \mathrm{FWHM}_{H\alpha}$ and use our integrated NIRSPEC line flux as a reference. With calibrated flux information,

we are in a position to derive SFR distributions for our objects.

5.4 Results

In this section we present our results for each individual target. We show Hα maps for each of our targets in Figs. 5.1-5.6. We rotated each of these images from the instrument position angle (PA) such that North is up and East points towards the left.

5.4.1 SMM J030227.73

SMM J030227.73 was first detected by Webb et al. (2003b) as part of the Canada-UK Deep Submillimeter Survey (CUDSS). Optical and near-IR spectra by C05 and S04 place this galaxy at $z \simeq 1.4076$. A high [NII]/Hα ratio ([NII]/Hα = 1.38$\pm$ 0.07; S04) and a broad Hα (FWHM$_{H\alpha}$ = 1500 $\pm$ 266 km s^{-1}; see Chapter 4) suggests that this SMG has significant AGN activity. These conclusions were confirmed by S06 with the Gemini-GNIRS integral field unit. Furthermore, *Spitzer* mid-IR spectroscopic follow-up of this object shows a substantial excess in mid-IR continuum, suggesting a significant AGN contribution (see Table 3.4; Menéndez-Delmestre et al. 2008).

We create a NB Hα image by collapsing the reduced data cube along the wavelength range $\simeq$ 1.57 $-$ 1.59 μm, centered around the redshifted Hα line corresponding to $z = 1.4076$. The resulting Hα emission map is shown in Fig. 5.1. On the bottom-left panel of Fig. 5.1 we overlay Hα contours on the *HST-ACS/NICMOS* true color image of SMM J030227.73, representing the *BVI*-band continuum of this galaxy. From the *HST* image we see that the continuum emission is dominated by a bright, compact source, which coincides with the compact ($\simeq 0.7''$) peak of Hα emission detected with OSIRIS. S06 detect compact Hα emission coinciding with what appears in the *HST* image as a secondary compact knot, $1.3''$ away from the central source (just off our OSIRIS FOV). They tentatively identify this second clump as an AGN, according to a high [NII]/Hα ratio.
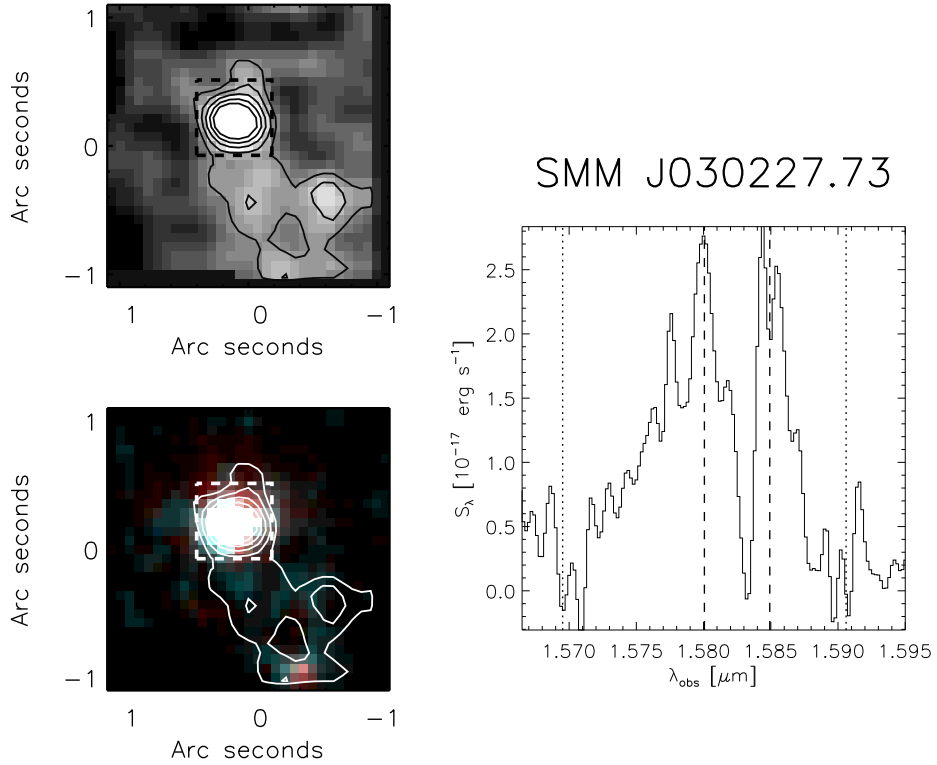
Figure 5.1 OSIRIS Hα detection in SMM J030227.73. (**Top Left:**) OSIRIS Hα emission integrated across the line with surface brightness contours overlaid (inner and outer contour $\sim 50, 10\sigma$). (**Bottom Left:**) The same σ-contours overlaid on a multicolor *HST*-NICMOS image of the galaxy. Note that there is substantial offset between the HST emission and the OSIRIS Hα emission. (**Right:**) Flux-calibrated 1D spectrum of Hα emission within the region indicated by the dashed box in the left panels. The redshifted wavelengths for Hα and $[\mathrm{NII}]_{6583}$ are indicated by the dashed lines. The dotted vertical lines denote the wavelength range over which we collapsed the OSIRIS cube to obtain the narrow-band Hα-[NII] image shown in the bottom left panel. We see that the central compact source displays a bright, broad Hα ($S_{H\alpha} = 1.023 \pm 0.06 \times 10^{-15}$ erg s^{-1} cm^{-2} Å^{-1}, FWHM$_{rest} = 1070 \pm 76$ km s^{-1}, with significant emission from the [NII] line ([NII]/Hα $= 0.53 \pm 0.1$).

With the aid of LGS-AO, OSIRIS allows us to resolve the region between these two compact components, in contrast to the S06 results, which distinguish no diffuse Hα emission. To the South-East of the central bright source in Fig. 5.1, OSIRIS intensity contours highlight a region of diffuse Hα emission that extends out to $\gtrsim 1''$.

In Fig. 5.2 we show the Hα S/N, line-width and velocity maps for SMM J030227.73. The bright, compact knot from the central source stands out at a $S/N > 30$ while the faint and diffuse emission appears at a lower, but still significant $S/N \sim 10 - 15$. We extract a 1D spectrum of the compact, bright region which reveals broad Hα emission (FWHM$_{rest} = 1070 \pm 76$ km s^{-1}), accompanied by a strong emission from the forbidden transition [NII]$_{6583}$ (see Fig. 5.1). From the spatial distribution of Hα line-widths in Fig. 5.2, we see the difference in Hα line characteristics between the compact and diffuse emitting regions, where the latter displays a much narrower component (FWHM$_{rest} = 110 \pm 15$ km s^{-1}). This suggests that the bright central source corresponds to an AGN (in agreement with S06), while the diffuse emission appears to be associated with spatially extended star formation. Since our OSIRIS observations do not cover the full extent of this secondary knot of emission we cannot test the possibility of two AGNs within this system.

The velocity map in Fig. 5.2 (bottom panel), measured relative to the rest-frame UV redshift identified by C05, suggests that the diffuse Hα component is offset from the compact component by $\simeq 150 \pm 50$ km s^{-1}.

5.4.2 SMM J123549.44

Long-slit near-IR observations of this source (S04) and ultra-deep *Chandra* images (Alexander et al. 2005a) have revealed clear AGN signatures. Furthermore, recent mid-IR observations have revealed an excess of hot continuum emission, in agreement with the hypothesis of a significant contribution from AGN activity to the bolometric luminosity (Menéndez-Delmestre et al. 2008). Tacconi et al. (2006, 2008) have also undertaken high-resolution CO observations of this galaxy. They found CO emission dominated by a compact source ($\lesssim 0.5''$) with a prominent double-peaked CO profile,
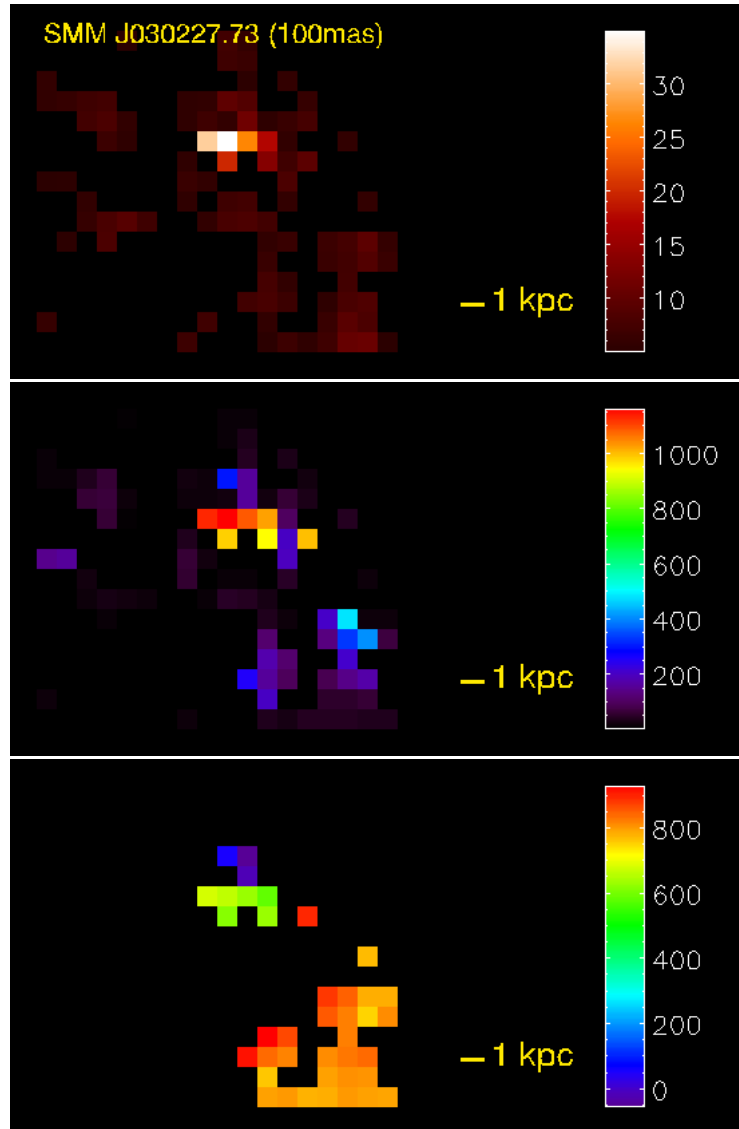
Figure 5.2 Distribution of Hα emission in SMM J030227.73. For all images, North is up and East is left. (**Top:**) S/N map displaying a bright compact source and additional lower-level extended emission. (**Middle:**) Hα line-width (σ_{rest}) map in units of km s^{-1}, showing that the central component has a rather broad (FWHM$_{H\alpha}$ $\simeq$ 1000 km s^{-1}) relative to the extended emission, with FWHM$_{H\alpha}$ $\lesssim$ 200 km s^{-1}. This distribution of line-widths suggests that the bright compact Hα emission in the center is associated with the broad-line region of a central AGN. Extended emission appears to be narrower and thus associated with star formation. (**Bottom:**) Hα velocity map, suggesting relative offsets $V_{rel} \simeq 200$ km s^{-1}. See §5.4.1 for details.
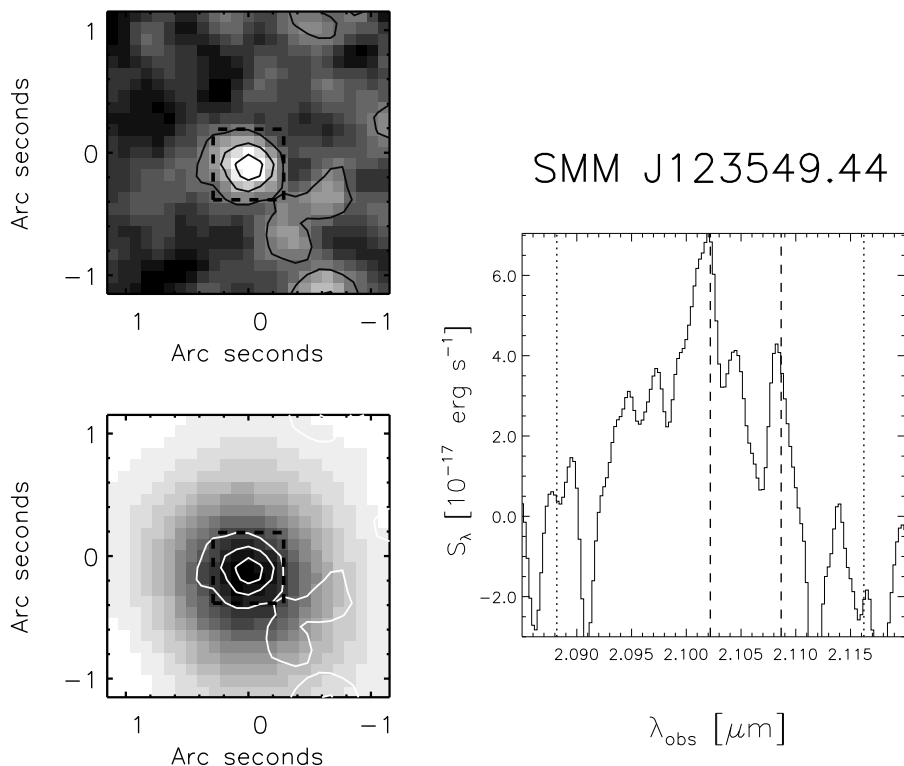
Figure 5.3 Hα emission as detected by OSIRIS in SMM J123549.44, following the same format as Fig. 5.1. The bottom left panel displays the Hα OSIRIS contours (the outermost representing the 5σ contours) overlaid on a *NICMOS I*−band image. We see that the Hα within the central $\sim 1''$ is dominated by a bright, compact source. Displaying a broad Hα line (FWHM$_{rest} \gtrsim 1000$ km s^{-1}), we take this emission knot to be associated with AGN activity.

which they associate with the orbital motions of gas within a disk close to the central AGN.

Optical and near-IR (long-slit) spectroscopy set this object at $z = 2.2032$ (C05, S04). The redshifted Hα line is thus expected at $\lambda = 2.1023$. We collapse the OSIRIS cube along the dispersion direction within $\Delta v \simeq 2000$ km s^{-1} and obtain the narrow-band Hα image presented in Fig. 5.3. The Hα emission for SMM J123549.44 is dominated by a compact ($\sim 0.7''$) source, though faint traces of diffuse emission extend out to $1''$ to the South-West of the central region (see also S/N map in Fig. 5.4). From long-slit observations, S04 report a relatively narrow Hα emission of FWHM$_{rest} \simeq 536$ km s^{-1} SMM J123549.44. However, we find that the integral
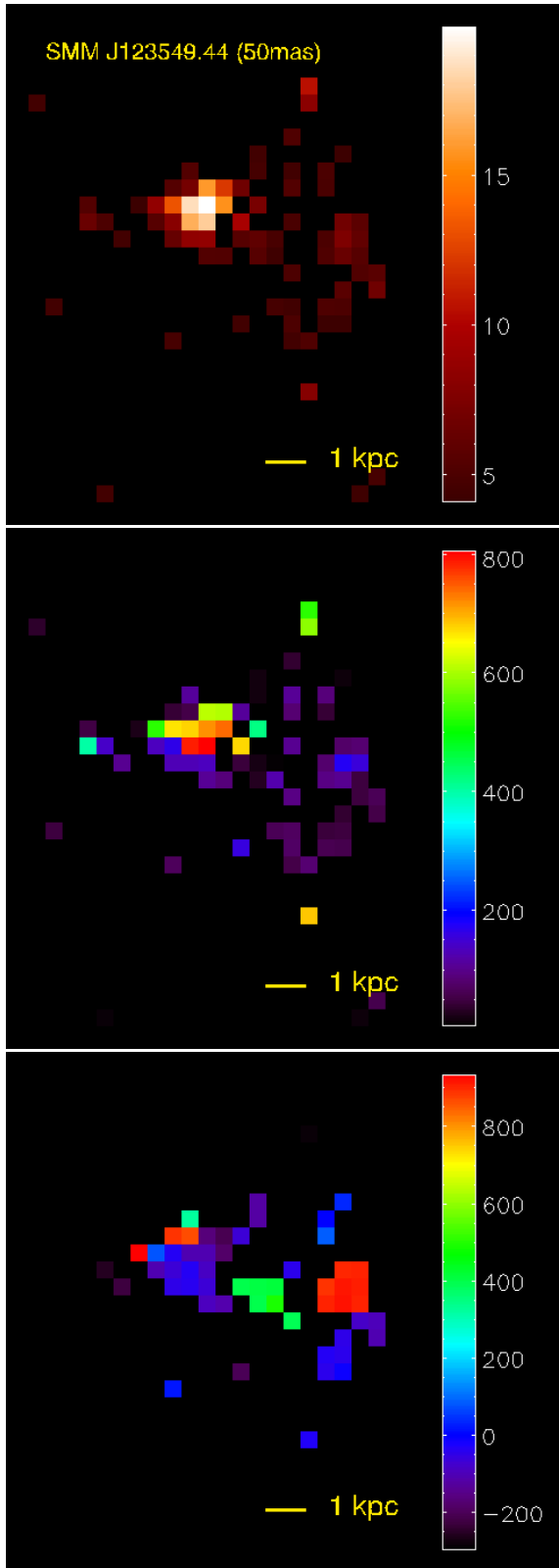
Figure 5.4 Distribution of Hα emission in SMM J123549.44, following the same format as Fig. 5.2. We see that the Hα emission is dominated by a compact source with broad Hα emission (FWHM$_{rest}$ = 1400 km s^{-1} or $\sigma \simeq 600$ km s^{-1}). At a fainter $S/N \simeq 5$, diffuse emission can be seen with narrower Hα line emission ($\sigma \lesssim 200$ km s^{-1}).

OSIRIS view of this object allows us to distinguish a rather broad Hα line from the central region indicated by the dashed box in Fig. 5.3, with FWHM$_{rest}$ $\simeq$ 1390 $\pm$ 50 km s^{-1} (or σ $\simeq$ 600 km s^{-1} in the middle panel of Fig. 5.4). The map of relative velocities (using z = 2.2032 as a reference; S04) suggests that there might be velocity offsets of up to 900 km s^{-1} within the diffuse region. Such large velocity offsets within this system may be attributed to the relative motion of multiple galactic-scale companions, potentially undergoing a merger. However, the low S/N of this trace remains an important caveat.

5.4.3   SMM J163650.43

This galaxy was first identified in the submm by Scott et al. (2002) and its broad-band near-IR emission has been studied in detail by Smail et al. (2003). With a bolometric luminosity L$_{bol}$ = $(3 \pm 2) \times 10^{13}$ L$_{\odot}$, this galaxy is unusually luminous even as an SMG (Chapman et al. 2003). Optical and near-IR spectroscopy revealed a redshift of $z \simeq 2.38$ and unveiled broad Hα emission (S04) and a high [OIII]/Hβ ratio, signatures characteristic of a Seyfert AGN (Smail et al. 2003). This galaxy has been resolved into different components, with its spatial extension and complex structure (Smail et al. 2003; S06).

With OSIRIS LGS-AO, we zoom into the inner regions of this galaxy. In Fig. 5.5 we show the OSIRIS data cube collapsed along the dispersion direction within a range Δv $\simeq$ 2000 km s^{-1} and centered at $\lambda \simeq$ 2.22 μm, where redshifted Hα is expected for this source. We find diffuse Hα emission extending over $\simeq (1'')^2$, in the shape of an arc. We overlay the OSIRIS intensity contours atop a true-color BVI-band HST-image to find that the Hα emission extends throughout the continuum light. We extract the 1D spectrum of a region enclosing the full extent of the Hα emission (box 2) and measure an intermediately broad Hα line with FWHM$_{rest}$ = 710 $\pm$ 50 km s^{-1}. A closer look at the distinct regions within this galaxy reveals that the ensemble emission is the result of a combination between a broad Hα region (box 1) and regions with narrow Hα emission (box 0), with FWHM$_{rest}$ = 2400 and 475 km s^{-1}, respectively.
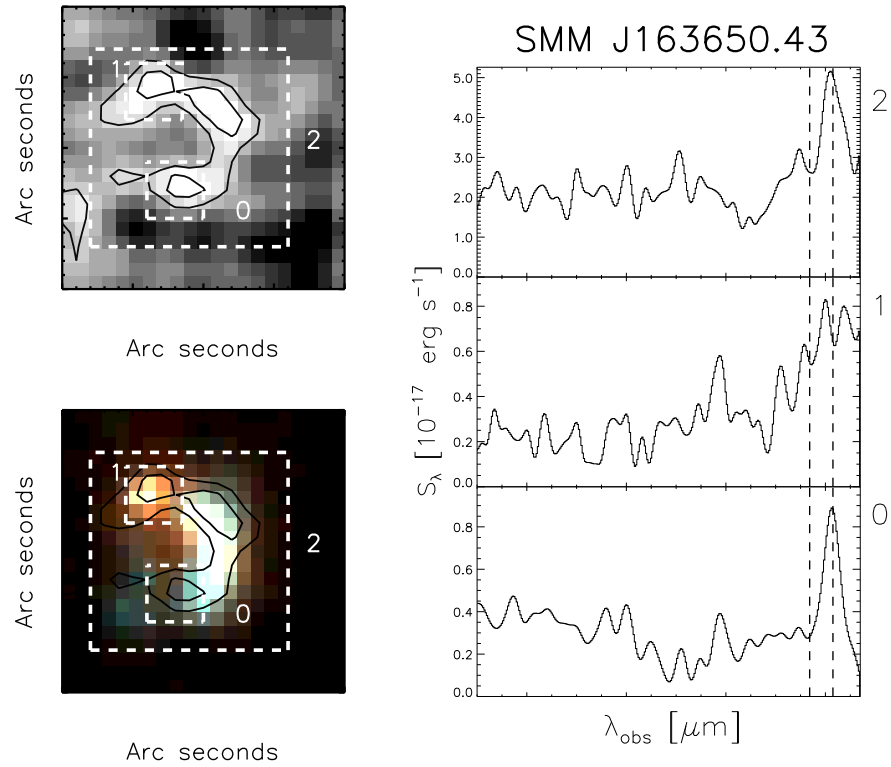
Figure 5.5 Hα emission as detected by OSIRIS in SMM J163650.43, following the same format as Fig. 5.1, with surface brightness contours in 2σ steps with the outermost contour corresponding to 8σ, overlaid on a multicolor *HST*-NICMOS image of the galaxy. The Hα intensity contours extend along the entire continuum-bright region in the *HST* image. We see that there is diffuse emission extending in the shape of an arc, within which Hα line characteristics differ: the north-east red clump in the *HST* image (box 1) displays a broad Hα line, while other regions of the diffuse emission display a narrow Hα line (box 0). See §5.4.3 for details.

The broad Hα emission coincides with the red knot visible in the underlying *HST* image, while the narrow Hα regions are associated with the diffuse emission to the south.

In Fig. 5.6 we show the S/N of the gaussian fits to the Hα line at each spatial pixel within the source. The southern and eastern extension of the arc-shaped region in the collapsed OSIRIS cube in Fig. 5.5 have modest S/N ($\sim 5-8$). This physically extended region corresponds to narrow Hα detection, as can be seen by the values of velocity dispersion $\sigma \simeq 200$ km s^{-1} (FWHM$_{rest}$ = 475 km s^{-1}; see Table 5.2) in the middle-panel of Fig. 5.6. On the other hand, the northern compact region with broad Hα emission (FWHM$_{rest}$ = 2400 km s^{-1}) suffers from low S/N (< 3). This reflects the greater ease of detecting a narrow emission line that emerges sharply from the continuum emission as compared with a broad emission feature (see Fig. 5.5). We do not find any velocity offset between the different components in this galaxy, as given by the centroids of the gaussian fits to the Hα line emission.

Prior long-slit spectroscopic work by S04 attempted to disentangle the broad and narrow Hα components. They distinguished narrow Hα component with an underlying broad component (FWHM$_{rest}$ $\simeq$ 306 $\pm$ 47 and 1753 $\pm$ 238 km s^{-1}, respectively). We emphasize that the long-slit spectroscopic view provides insight solely to the integrated emission from the region enclosed within the slit. Contributions to the Hα emission arising from the AGN are mixed with extended emission arising from star-forming regions. Therefore, it is very challenging to separate reliably these two contributions. With OSIRIS we are able to separate reliably spectra of spatially distinct regions within a galaxy. This separation between spatial and spectral information allows us to derive reliable dynamical masses and SFRs, uncontaminated by the broad-line region of an AGN. We discuss this in §5.5.1 and §5.5.2.

5.5   Discussion

Recent near-IR integral field spectroscopic observations by S06 have shown that most SMGs often have multiple components that can be spatially distinguished within the
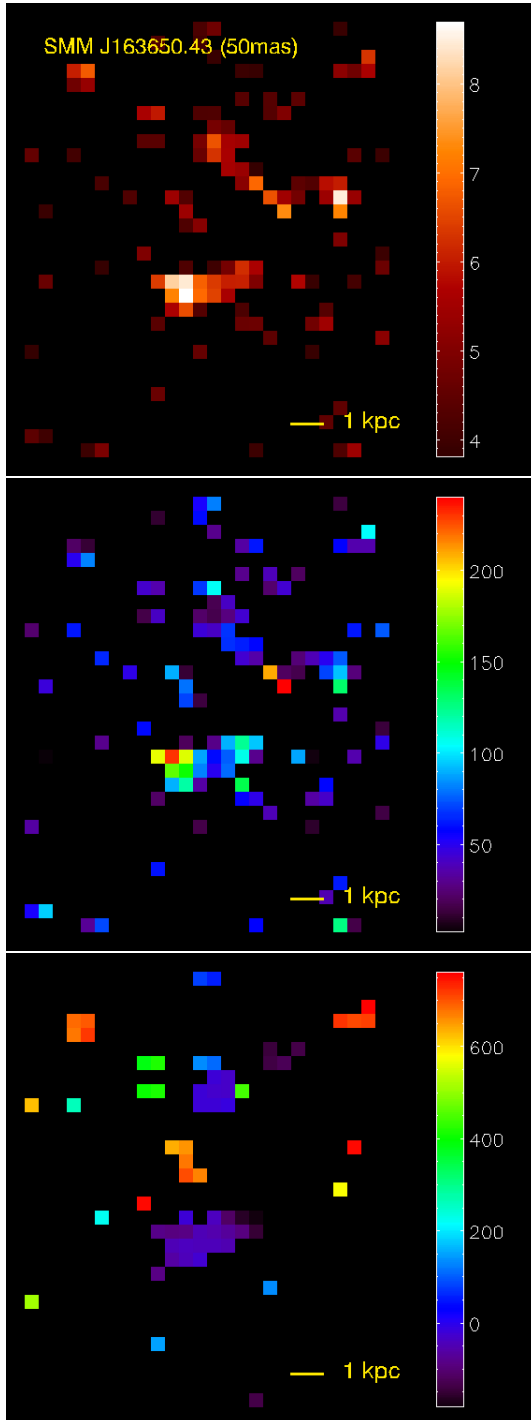
Figure 5.6 Distribution of Hα emission in SMM J163650.43, following the format of Fig. 5.2. We note that the S/N-map shows very weak detection of the region corresponding to the broad Hα region. It is more difficult to detect a broad, shallow line atop a continuum than it is to detect a narrow line. These maps show precisely this: the northern clump with broad Hα (see Fig. 5.5) does not appear in these maps, while the southern region, with narrower Hα ($\sigma \simeq 200 \, \text{km s}^{-1}$) stands out clearly.

central ~ 8 kpc. With OSIRIS we have been able to peer into these central regions, allowing us to zoom further in than these previous integral field observations without LGS-AO corrections.

From the global dynamics revealed by the integral view of our SMG targets, we find no indication that gas kinematics are associated with ordered motions, as would be present in a gaseous disk. This is in contrast to relatively recent reports on high-redshift LBGs (Förster Schreiber et al. 2006; Law et al. 2007), where continuous, gradual velocity gradients have been identified in individual cases as evidence for ordered rotation. SMGs do not appear to host such ordered kinematics: we find velocity offsets between distinct components, but no continuous velocity structure across SMGs. These results strengthen the conclusion derived from deep rest-frame optical *HST*-imaging that SMGs are disturbed systems, likely corresponding to a merger (Smail et al. 1998, 2004). Within this context the distinct components that comprise the SMGs could potentially be associated with the remnants of the pre-merger galaxies.

We have been able to spatially distinguish regions with broad Hα emission that are dominated by AGN activity and those with narrow Hα emission where star formation is taking place. Diffuse, narrow Hα emission – where star-formation activity dominates – extends over $\sim 0.7 - 2''$ (see Table 5.2). At the redshifts covered by our targets, these angular sizes correspond to $8 - 17$ kpc. These sizes compare reasonably well to those presented by S06 and Tecza et al. (2004), who report resolved nebular emission on scales from $4 - 11$ kpc for a total of seven SMGs. With these sizes in hand, we are in a position to derive reliable SFRs – keeping Hα flux calibration caveats in mind – and clean estimates of dynamical masses as traced by the Hα emission from the ionized gas distribution in regions with no AGN contribution (see §5.5.1).

5.5.1 Dynamical Masses

The kinematics of the gas, as given by the velocity dispersion (σ) of rest-frame optical lines, can be used to estimate dynamical masses. This relies on the assumption
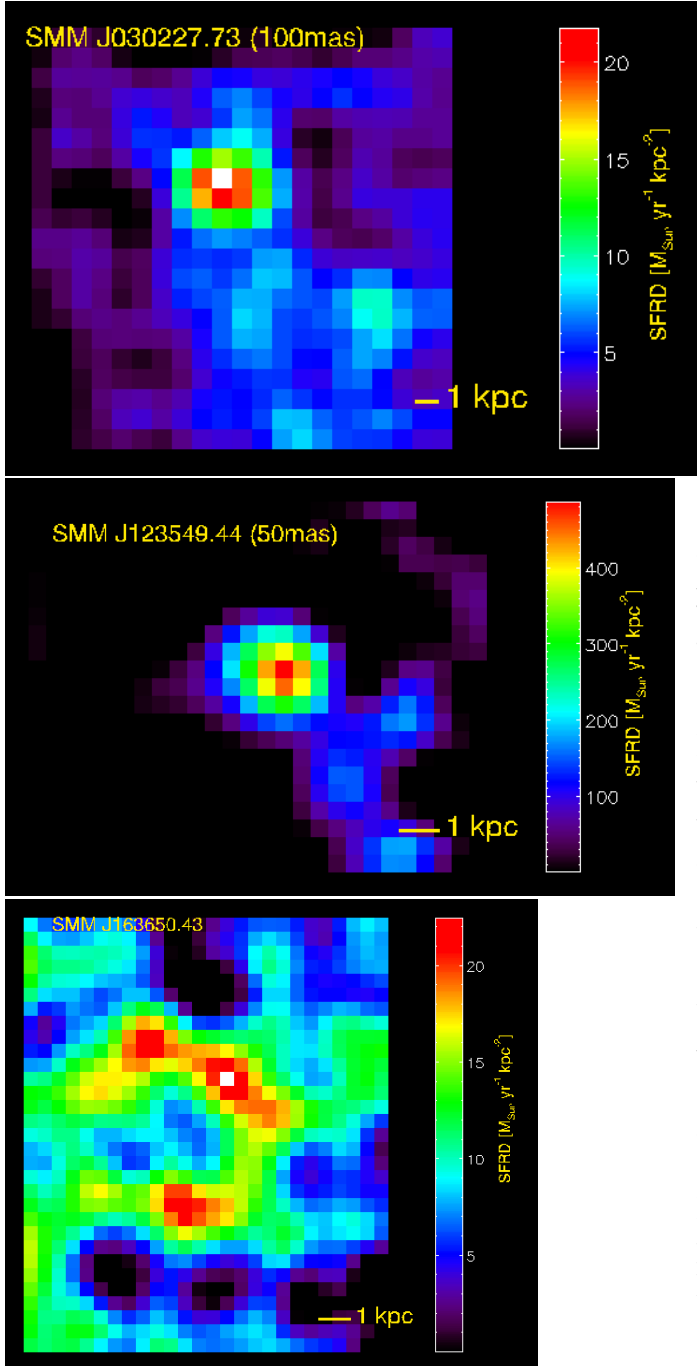
Figure 5.7 Map of SFR surface densities (Σ_{SFR}) in units of $M_\odot$ yr^{-1} kpc^{-2} for our three SMG targets: (**Top:**) SMM J030227.73, (**Middle:**) SMM J123549.44 and (**Bottom:**) SMM J163650.43. We have estimated a typical extinction correction and applied it to these maps (see §5.5.2 for details). SMM J030227.73 and SMM J123549.44 are dominated by a compact region of broad Hα associated with an AGN. In both cases, diffuse emission towards the south-western direction appears to be composed of several compact knots, ~ 1 kpc in size. SMM J163650.43 displays a very large spatial extension, also comprised of compact knots of $\sim 1-2$ kpc in size.

that line broadening is due to the internal dynamics of the gas within the galaxy's central potential well. However, in the presence of an AGN – and depending on the geometrical orientation of the object – the large velocities intrinsic to the gas within the AGN's broad-line region may enhance the width of rest-frame optical lines by confusion. The resulting mixing of gas kinematics contained by rest-frame optical lines makes it quite challenging to disentangle the AGN and the stellar contributions through long-slit spectroscopy, and can lead to significant overestimates in dynamical masses and SFRs. Since a number of AGN signatures have been revealed in X-ray, optical and mid-IR observations of individual SMGs (e.g., Alexander et al. 2005a, C05, Menéndez-Delmestre et al. 2008), this is a critical consideration to take into account.

With OSIRIS we can rely on the line-width of the Hα emission of regions uncontaminated by an AGN to derive reliable dynamical masses. For this, we use Equation 4.5, where σ is the velocity dispersion of the gas and R is the radial size of the gas distribution. We use velocity dispersions of the regions displaying no AGN signatures (referred to as *diffuse* emission regions in Table 5.2) and consider the full spatial extension of the Hα emission in determining the radial size of the gas distribution. In this manner, we estimate a dynamical mass for each galaxy as a whole assuming that the gas dynamics are reflected by the line-width of the narrow Hα line observed in the regions uncontaminated by the broad-line region of an AGN. We find dynamical masses $M_{dyn} = (4.3 \pm 0.6) \times 10^{10}$ M$_\odot$ and $M_{dyn} = (2.0 \pm 0.5) \times 10^{11}$ M$_\odot$ for SMM J030227.73 and SMM J163650.43, respectively. In the case of SMM J123549.44, OSIRIS only detects marginally faint diffuse emission, and so we do not estimate a dynamical mass.

Assuming typical sizes of $\sim 0.5 - 1''$ or $4 - 8$ kpc, S04 find a typical mass of M$_{dyn} \sim (1 - 2) \times 10^{11}M_\odot$ for SMGs. For SMM J163650.43, they distinguish a narrow Hα component with FWHM$_{rest} = 306 \pm 47$ km s^{-1} which translates into a dynamical mass $M_{dyn} = (1.62 \pm 0.50) \times 10^{11}$ M$_\odot$ using Equation 4.5. This value agrees with our spatially resolved result (see Table 5.2). S04's NIRSPEC observations of SMM J030227.73, uncorrected for any AGN contamination to the integrated broad

Hα emission detected suggest a dynamical mass M$_{dyn}$ = $(3.15 \pm 0.23) \times 10^{11}$ M$_\odot$. By excluding the contamination from AGNs to the width of the Hα line, our OSIRIS results lead to a significantly lower and more reliable dynamical mass than that derived in long-slit observations.

From Fig. 5.7 we can see that the Hα emission within the diffuse region is concentrated in 2–3 multiple clumps. Due to the low S/N of the Hα line in these individual components, we cannot derive explicitly dynamical masses for the individual clumps. We compare sizes and σ-values for these regions to those reported for LBGs by Erb et al. (2003) and Law et al. (2007): for the three SMGs in our sample we find that with values of $\sigma_{rest} \lesssim 200$ km s^{-1} within the regions of diffuse emission and clump sizes $R \sim 1$ kpc (see middle panel in Figs. 5.2, 5.4, 5.6 and Fig. 5.7). The individual clumps that compose the diffuse emission in SMGs thus have similar properties to that of individual LBGs. We come back to this discussion in the following section.

Greve et al. (2005) report dynamical masses in the range M_{dyn} = $0.3-37 \times 10^{10}$ M$_\odot$ derived from CO (3-2) observations in a large sample of 18 SMGs. Similar results have been obtained from high-resolution CO observations by Neri et al. (2003) and Tacconi et al. (2006, 2008). We do not have a direct comparison to the dynamical masses measured in CO for SMM J030227.73 or SMM J163650.43, but our results are consistent with the range of lower limits from CO masses found for SMGs. The similarity in these results suggest that the molecular gas – as traced by CO – and the ionized gas – traced by the Hα emission to which we have unique spatially-resolved access with OSIRIS – both appear to map similar baryonic dynamics.

5.5.2   Hα Sizes and Gas Masses

The integral field view of Hα emission in a galaxy can give us clues as to the distribution of star-formation activity per projected area, by associating the Hα integrated line flux at each pixel with a local SFR, following Equation 5.1, taking into account the pixel scale (50 mas or 100 mas) used for the OSIRIS observations. In Fig. 5.7 we show maps of (projected) SFR surface densities (Σ_{SFR}) for the three SMGs in our

Table 5.2. Summary of *OSIRIS* IFU Results

	SMM J030227.73	SMM J123549.44	SMM J163650.43
z_{opt}	1.408	2.203	2.378
$z_{H\alpha}$	1.4076	2.2032	2.385
$S_{H\alpha}$ (broad) [erg s^{-1} cm^{-2}]	$1.02 \pm 0.06 \times 10^{-15}$	$5.35 \pm 0.13 \times 10^{-15}$	$1.04 \pm 0.06 \times 10^{-15}$
$S_{H\alpha}$ (narrow) [erg s^{-1} cm^{-2}]	$0.59 \pm 0.04 \times 10^{-15}$	–	$0.25 \pm 0.03 \times 10^{-15}$
FWHM$_{rest}$ (broad) [km s^{-1}]	1070 ± 76	1390 ± 50	2400 ± 134
FWHM$_{rest}$ (narrow) [km s^{-1}]	110 ± 15	–	475 ± 60
$[NII]/H\alpha$	0.53 ± 0.1	0.2 ± 0.1	–
SFR$_{diffuse}$ [M$_\odot$ yr^{-1}] [a]	293 ± 10	278 ± 82	559 ± 23
Σ_{SFR} [M$_\odot$ yr^{-1} kpc^{-2}] [b]	1.38 ± 0.37	–	4.76 ± 0.42
Size $_{compact}$	$0.7 \times 0.7''$	$0.7 \times 0.7''$	$0.4 \times 0.4''$
	6×6 kpc^2	5.9×5.9 kpc^2	3.3×3.3 kpc^2
Size $_{diffuse}$	$1.1 \times 1.5''$	$1.1 \times 0.7''$	$1 \times 1''$
	9.4×12.8 kpc^2	9.2×5.9 kpc^2	8.3×8.3 kpc^2
Size $_{total}$	$2.0 \times 1.7''$	$1.3 \times 0.9''$	$1 \times 1''$
	17.0×14.5 kpc^2	10.9×7.5 kpc^2	8.3×8.3 kpc^2
M$_{dyn}$ [M$_\odot$]	$(4.3 \pm 0.6) \times 10^{10}$	–	$(2.0 \pm 0.5) \times 10^{11}$
M$_{gas}$ [M$_\odot$] [c]	$(2.5 \pm 0.7) \times 10^{10}$	$(9.0 \pm 0.6) \times 10^{10}$	$(3.5 \pm 1.4) \times 10^{10}$

[a] Observed SFRs as measured from the observed Hα line, not corrected for extinction.

[b] SFR surface densities within the diffuse region, from the Hα-derived SFR at each pixel, divided by the pixel area.

[c] Gas masses derived from our extinction-corrected Σ_{SFR}, assuming the Schmidt-Kennicutt relation. We correct for the expected overestimate resulting from the inherent assumption of a H$_2$–CO conversion factor appropriate for normal galaxies, rather than ULIRGs. See §5.5.2 for details.

sample, corrected for extinction based on typical Balmer decrements found in SMGs (Takata et al. 2006; see §4.5.2 for details).

We find extinction-corrected SFR surface densities $\Sigma_{SFR} \sim 10-100$ M$_\odot$ yr^{-1} kpc^{-2} within the regions of diffuse emission in SMM J030227.73 and SMM J163650.43. These values set SMGs within the high range of Σ_{SFR} values found for local circumnuclear starbursts, but $2-3$ orders of magnitude higher than in normal spirals (see Fig. 9 in Kennicutt 1998). They are also on the high end of the Σ_{SFR} distribution for the optically-selected LBGs (see Law et al. 2007), and significantly higher than the LBG median, $< \Sigma_{SFR} >= 2.9$ M$_\odot$ yr^{-1} kpc^{-2} (see Fig. 3 in Erb et al. 2006a). Note that the SMGs in our sample exhibit SFR surface densities that remain *below* the highest values of Σ_{SFR} found in local starbursts by approximately two orders of magnitude. These results, together with the spatially-extended Hα distribution $\gtrsim 1''$, suggests that SMGs have similar intermediately high rates of star formation as local circumnuclear starbursts. However, SMGs appear to be undergoing this intense activity on

much larger spatial scales, reflecting their much greater luminosity.

By tracing the regions undergoing star formation, the distribution of (narrow-line) Hα emission can also provide us with a mapping of the star-forming molecular and presumably gas-rich regions that fuel this activity. Even though CO observations have a direct view of the distribution of molecular gas throughout a galaxy, the ionized gas surrounding massive stars is expected to mix with the molecular gas medium, thus giving an additional window to characterize the molecular gas budget of a galaxy. We assume the validity of the local Schmidt Law presented by Kennicutt (1998) (hereafter, the *Schmidt-Kennicutt* relation) to associate the global SFR surface density with the gas surface density (Σ_{gas}) in these galaxies:

$$\Sigma_{\mathrm{SFR}} = (2.5 \pm 0.7) \times 10^{-4} \times (\Sigma_{\mathrm{gas}})^{1.4 \pm 0.15}, \tag{5.2}$$

where Σ_{SFR} is in units of [M$_\odot$ yr^{-1} kpc^{-2}] and Σ_{gas} in [M$_\odot$ pc^{-2}]. When referring to *gas* masses, we assume that the molecular gas component comprises the bulk of the total gas. This is a reasonable assumption, as it has been shown that in nearby starbursts the atomic gas comprises less than a few percent of the total gas mass (e.g., Sanders & Mirabel 1996).

We note that the Schmidt-Kennicutt relation relies – for the sake of simplicity – on the assumption that a common CO-to-H$_2$ conversion factor can be used for all galaxies (see Kennicutt 1998). In particular, it assumes a conversion factor valid for nearby normal galaxies, M(H$_2$)= $X_{CO} L'_{CO(1-0)}$, where $X_{CO} \simeq 4.6$. However, the validity of this assumption is disputed: this conversion factor systematically overestimates gas masses in local ULIRGs (Solomon & Vanden Bout 2005). The physical basis for the CO-to-H$_2$ relation in normal galaxies relies on the assumption that molecular gas principally lies within gravitationally bound, virialized clouds. In the case of ULIRGs, a more appropriate gas-distribution model is that of CO emission arising from an intercloud medium, so that CO kinematics not only reflect gas masses, but also dynamical masses from stars intermixed in this medium. Hence, a conversion factor $X_{CO} \simeq 0.8$ K km s^{-1} pc^2 has been adopted as a more appropriate conversion

factor for ULIRGs (see also Tacconi et al. 2008). Taking this into account, we assume that gas masses calculated from the Σ_{gas} derived from the Schmidt-Kennicutt relation will likely be overestimated by a factor of $\sim 4.6/0.8 \simeq 6$.

Keeping these caveats in mind, we use the Schmidt-Kennicutt relation to estimate gas densities and assuming a typical Hα extinction correction for SMGs (see §4.5.2), we obtain $\Sigma_{gas} \sim 10^3 - 10^4$ M$_\odot$ pc^{-2}, similar to the findings of Greve et al. (2005) and Tacconi et al. (2006, 2008) based on CO observations of SMGs. For the observed sizes over which we detect nebular emission and considering the caveats discussed above, we estimate gas masses $M_{gas} \sim \Sigma_{SFR} \times R^2 = (2.5 \pm 0.7), (9.0 \pm 0.6)$, and $(3.5 \pm 1.4) \times 10^{10}$ M$_\odot$ for SMM J030227.73, SMM J123549.44 and SMM J163650.43, respectively. The quoted errors correspond to the deviation in flux values found within the extended region of emission. More accurate uncertainties are estimated to amount to $\gtrsim 30\%$.

These gas masses are similar to those found in LBGs ($< M(H_2) >= 3.0 \times 10^{10}$ M$_\odot$ within a typical radius of ~ 2 kpc; see Erb et al. 2006b; Law et al. 2007). Furthermore, CO interferometric observations of low-redshift ULIRGs show that such extreme local objects are also gas-rich, M(H_2) $\sim 10^9 - 4 \times 10^{10}$ M$_\odot$, with typical spatial extensions of $\lesssim 1$ kpc (e.g., Young & Scoville 1991). Therefore, even though SMGs appear to be just as or even more gas-rich than these other galaxy populations, the typical sizes over which molecular gas extends for SMGs are significantly larger, though some of the brightest and most massive LBGs do appear to have more comparable Hα spatial extensions ($R_{H\alpha} \sim 2 - 7$ kpc; Förster Schreiber et al. 2006).

Together with the finding that SFR surface densities in SMGs are similar to those found in circumnuclear starbursts and higher than those in LBGs, these gas masses suggest that SMGs are consuming their available gas rapidly. With extinction-corrected SFRs from the diffuse regions in SMGs $\sim 1000 - 2000$ M$_\odot$ yr^{-1}, we estimate that SMGs will deplete their gas reservoirs on a timescale of M_{gas}/SFR$\simeq 10^8$ yr. Considering the short gas-depletion timescale, this suggests that the SMG phase represents a very short episode in the evolution history of a galaxy.

5.5.2.1   Comparison to CO-Derived Gas Masses

The gas masses we estimate agree with the average value determined from CO observations of SMGs (Greve et al. 2005; Tacconi et al. 2006, 2008). Assuming a CO-to-H_2 conversion factor appropriate for local ULIRGs, Greve et al. (2005) measure a median molecular gas mass $< M(H_2) > = (3.0 \pm 1.6) \times 10^{10}$ $M_\odot$. Tacconi et al. (2008) undertook high-resolution CO observations of four SMGs, including SMM J123549.44, and found $M_{gas}(CO) = (4 \pm 0.5) \times 10^{10}$ $M_\odot$ for SMM J123549.44, comparable with our result.

We note that CO observations typically target high-J ($J \geq 2$) CO transitions, rather than the lowest (1-0) transition. The former trace warm and dense gas, while the latter trace the likely more abundant and colder gas. Hainline et al. (2006) reported the first detection of CO(1-0) emission from SMM J13120+4242 with the Green Bank Telescope, deriving a cold molecular gas mass of $M_{CO(1-0)} = 1.6 \times 10^{11}$ $M_\odot$, four times larger than that derived from the higher CO(4-3) transitions (Greve et al. 2005). This suggests that a large fraction of molecular gas is likely left unaccounted for when tracing CO through the higher J-transitions and that the true gas masses are likely closer to 4× these higher-J estimates.

There are also important caveats to keep in mind when relying on the ionized gas to map the distribution of gas across a galaxy, three which we briefly mention here. First, even though in the near-IR we are less prone to dust obscuration than in the optical, dust extinction is still an important factor. We have accounted for attenuations in observed Hα luminosities considering the typical optical depth derived from the Balmer decrement in SMGs (Takata et al. 2006). However, dust extinction in excess of the Balmer decrement would likely translate into lower estimates for gas masses. Second, our observations are limited to the OSIRIS FOV, such that we do not see the extent of the ionized gas beyond a radial distance of $R \sim 1-2''$ or $8-16$ kpc from the center. The third caveat we note is that our observations are only sensitive to regions with the highest surface brightness, ignited by massive star formation. Therefore, our gas estimates are likely lower limits that fail to uncover the full extent of the gas

reservoir in these galaxies, which is likely traced to a better degree by CO observations of low-J transitions. However, even with these caveats in mind, the consistency of CO-derived gas mass estimates for SMGs with our Hα-derived values suggests that the spatial scale of ionized gas may be a viable venue to explore the distribution and abundance of gas fueling in high-redshift star-forming galaxies. Furthermore, recent high-resolution CO observations have shown that the CO emission can be displaced (and sometimes completely disjoint) from the distribution of the ionized gas (see Fig. 3 in Tacconi et al. 2008 for a clear example). This enigmatic result shows that we are only starting to unveil the intricacies of the gaseous kinematics within these galaxies. This motivates further the use of AO to probe the details of the distribution of the near-IR emitting gas.

With the gas masses derived from the extinction-corrected Hα emission (see Table 5.2) and considering the stellar masses derived from broad-band photometry ($M_{stellar} = 2.51 \pm 2.65 \times 10^{11}$ M$_\odot$; Borys et al. 2005), we estimate an average gas fraction of $< M_{\mathrm{gas}}/M_{stellar} > \sim 0.1 - 0.4$. If we consider the gas masses derived from CO emission (Greve et al. 2005) and boosted by the factor of four suggested by the work from Hainline et al. (2006), this gas fraction increases to ~ 0.5 (see also Neri et al. 2003). These results reinforce the conclusion that SMGs are gas-rich systems.

The preponderance of multiple galactic-scale sub-components in SMGs – as revealed by CO and both our IFU observations and those of S06 – together with the disturbed morphology reminiscent of interacting systems (Smail et al. 2004) suggests that SMGs are likely the result of merging episodes between gas-rich galaxies. LBGs have also been found to have large gas fractions $\sim 50\%$ (Erb et al. 2006b). Putting this together with the similar velocity dispersions and Hα emission sizes found in the individual clumps comprising the diffuse emission in SMGs to that of individual LBGs, these results suggest that the mergers in SMGs resemble mergers of $2 - 3$ 'LBG-like' sub-units.

5.6   Conclusions

We present the first integral-field spectroscopic LGS-AO observations on SMGs. We distinguish spatially the compact broad-Hα emission associated with an AGN and the extended narrow-Hα emission associated with star formation. We have thus improved our understanding on the internal dynamics of this enigmatic galaxy population and make reliable estimates of SMG masses and SFRs, uncontaminated by AGN and star formation mixing of rest-optical lines.

We do not find any indication of ordered motion within our targets. We find relative velocities of a few 100 km s^{-1} between galactic-scale sub-components in two of our targets, suggesting that these might be the remnants of originally independent systems undergoing a merger. Even after eliminating the influence of AGN activity, we measure large extinction-corrected SFRs $\sim 1000 - 2000$ M$_\odot$ yr^{-1} and large gas masses $M(H_2) \sim 10^{10}$ M$_\odot$. These gas masses are similar to those found in local ULIRGs and high-redshift LBGs, but the spatial extent over which Hα emission extends is significantly larger in SMGs, $\sim 8 - 16$ kpc. Furthermore, SMGs display similar SFR surface densities to local circumnuclear starbursts. All of these results taken together suggest that the submillimeter phase denotes a short-lived flaring-up of large spatial extension across these systems that rapidly depletes the available gas through intense star formation.